Check for updates

Numerical–experimental observation of shape bistability of red blood cells flowing in a microchannel†

Achim Guckenberger, ‡*[a] Alexander Kihm, ‡[b] Thomas John,[b] Christian Wagner §[bc] and Stephan Gekle §[a]

Red blood cells flowing through capillaries assume a wide variety of different shapes owing to their high deformability. Predicting the realized shapes is a complex field as they are determined by the intricate interplay between the flow conditions and the membrane mechanics. In this work we construct the shape phase diagram of a single red blood cell with a physiological viscosity ratio flowing in a microchannel. We use both experimental *in vitro* measurements as well as 3D numerical simulations to complement the respective other one. Numerically, we have easy control over the initial starting configuration and natural access to the full 3D shape. With this information we obtain the phase diagram as a function of initial position, starting shape and cell velocity. Experimentally, we measure the occurrence frequency of the different shapes as a function of the cell velocity to construct the experimental diagram which is in good agreement with the numerical observations. Two different major shapes are found, namely croissants and slippers. Notably, both shapes show coexistence at low (<1 mm s^{-1}) and high velocities (>3 mm s^{-1}) while in-between only croissants are stable. This pronounced bistability indicates that RBC shapes are not only determined by system parameters such as flow velocity or channel size, but also strongly depend on the initial conditions.

1 Introduction

Red blood cells (RBCs) are the major constituent of mammalian blood and therefore determine the majority of its flow properties. One of the most amazing features of RBCs is their deformability, allowing them to squeeze through channels with diameters much smaller than their own equilibrium size.[1–3] Another consequence of their deformability is the wide range of stationary and non-stationary shapes assumed by the RBCs in microchannel flows with dimensions similar to or slightly larger than the RBC equilibrium radius.[4–6] Understanding and being able to predict these shapes is of high importance

[a] Biofluid Simulation and Modeling, Theoretische Physik, Universität Bayreuth, Germany. E-mail: achim.guckenberger@uni-bayreuth.de; Tel: +49 921 55 4472
[b] Experimental Physics, Saarland University, Saarbrücken, 66123, Germany
[c] Physics and Materials Science Research Unit, University of Luxembourg, Luxembourg

‡ A. Guckenberger and A. Kihm contributed equally to this work.
§ S. Gekle and C. Wagner contributed equally to this work.

for a variety of reasons. From a fundamental point of view, it serves as the foundation in a bottom-up approach to understand the properties of red blood cell suspensions which are chiefly determined by single particle behavior.[7–13] From an applied perspective, a series of recent investigations have devised promising approaches for sorting cells based on their mechanical properties either in lateral displacement devices[14] or using high-speed video microscopy.[15] Finally, knowledge of the precise cell shape is also essential for accurately measuring geometric properties of cells.[16]

The most frequently observed shapes of RBCs in microchannel flows are the so-called "croissant" and "slipper" shapes. Examples are depicted in Fig. 1. Some researchers refer to croissants also as parachutes, although here we prefer the term croissant since our shapes are not perfectly rotationally symmetric (similar to the ones found by Farutin and Misbah[17]). Probably one of the earliest experimental studies on isolated red blood cells in flow was performed by Gaehtgens *et al.*,[18] where slippers as well as parachutes have been found depending on the diameter of the cylindrical channel. Suzuki *et al.*[19] presented an *in vivo* phase diagram of parachutes and slippers as a function of velocity and confinement. Slippers dominated at smaller diameters and higher velocities. Secomb *et al.*[20] compared experiments with 2D simulations in cylindrical
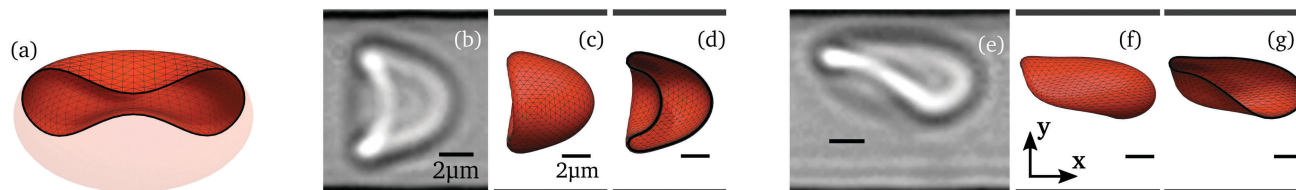
Fig. 1 Typical RBC shapes from simulations and experiments. (a) The typical discocyte shape employed in some of the simulations as the starting shape. Half of it was made transparent for illustration purposes. Its horizontal diameter is 8 μm. (b) A typical croissant observed in the experiments when applying a pressure drop of 100 mbar (cell velocity 0.98 ± 0.07 mm s^{-1}). (c) A croissant with a velocity of ≈ 1.1 mm s^{-1} obtained from the numerical simulations. (d) The cross-section of the croissant from (c). (e) A slipper from the experiments at 500 mbar (cell velocity 5.16 ± 0.11 mm s^{-1}). (f) A typical slipper from the simulations with a cell velocity of ≈ 5.2 mm s^{-1}. (g) The cross-section of the slipper from (f). The black lines on the shapes from the simulations depict the mesh. The bottom and top black lines in all figures are the walls (L_y ≈ 12 μm apart), while the small black lines are scale bars of length 2 μm. The flow is in the positive x-direction (except in figure (a) where no flow exists).

channels of 8 μm diameter for a cell velocity of approximately 1.25 mm s^{-1}. Furthermore, two other publications[21,22] considered the flow of RBCs at very low viscosity ratios of $\lambda \lesssim 0.27$. They presented a phase diagram showing parachutes and slippers, where the velocity was varied in the very high regime of 10 to 170 mm s^{-1}. Tomaiuolo et al.[23] found parachutes at smaller and slippers at higher velocities in cylindrical channels of 10 μm diameter. A subsequent study[24] as well as Prado et al.[26] considered the transient during start-up of the flow. Cluitmans et al.[26] detected croissants at lower ($\lesssim 5$ mm s^{-1}) and slippers at higher velocities ($\gtrsim 10$ mm s^{-1}) in rectangular channels with widths ≤ 10 μm. Moreover, Quint et al.[27] found a stable slipper and a metastable croissant at the same set of parameters in a wider channel of 25 μm × 10 μm. Other publications presenting experiments in channel flow also touch the subject of RBC shapes but focus on other aspects such as the methodology,[28–35] dense suspensions and cell interactions[18,22,35–42] or use vastly larger channel diameters.[13,43]

Numerical simulations and semi-analytical calculations of isolated particles in microchannels mostly studied axisymmetric RBCs[44–46] or 2D vesicles.[5,6,47–52] The numerical work by Aouane et al.,[5] for example, identified a large amount of dynamics including deterministic chaos. The first full 3D simulation of a single cell with a realistic RBC model (but with a ratio of inner to outer viscosity of $\lambda = 1$) was conducted by Noguchi and Gompper[53] who used a cylindrical tube with a diameter of 9.2 μm. They found the typical discocyte shape below and parachutes above a critical velocity which depends on the elastic parameters. A subsequent study by the same group additionally explored this threshold as a function of confinement.[54] Moreover, Fedosov et al.[4] presented very detailed phase-diagrams where the velocity and confinement was varied for three different sets of elastic moduli and a viscosity ratio of $\lambda = 1$. They observed four distinct regions where snaking, tumbling, slippers and parachutes occurred. Recently, Ye et al.[55] considered the shapes of an RBC with $\lambda = 1$ in rectangular microchannels (with width 10 μm and aspect ratios 1 to 2) for the three cell velocities 4, 20 and 100 mm s^{-1} and observation times up to ≈ 0.03 s. Snapshots after this short initial transient showed parachutes or slightly slipper-like shapes.

Bistability, i.e. the observation of two different stable shapes depending on the initial condition but at otherwise identical system parameters, was barely considered so far. It was observed for simpler situations such as close-to-spherical vesicles in unbounded Poiseuille flow analytically[56] and numerically[17] or near a single wall,[57] for a 2D RBC model in bounded Poiseuille flow,[20] for the initial transient of a red blood cell in a rectangular channel[55] or for simple shear flows.[13,58–60] No systematic experimental investigations exist for cells flowing in microchannels. Moreover, the 3D simulations and experimental investigations that were mentioned above and that consider the RBC shapes in microchannels in more detail all used a viscosity ratio of $\lambda \leq 1$, although analytical and numerical computations showed that choosing a physiologically more realistic value of $\lambda \approx 5$[61] can significantly affect RBC dynamics.[6,17,50,56]

Here we present a detailed systematic experimental-numerical study on the steady-state shape of isolated red blood cells in a rectangular microchannel. We use the physiological viscosity ratio of $\lambda = 5$ appropriate for healthy human red blood cells in the microcirculation.[61] The initial position is varied in the simulations directly, while experimentally we determine it via measurements at the channel entrance. Our central finding is that the initial starting position of the RBC has a decisive influence on the final steady-state shape of the red blood cell.

We begin by outlining our experimental and numerical methods in Section 2. Afterwards, the results from our experiments (Section 3) and simulations (Section 4) are presented, while Section 5 is dedicated to their detailed comparison. Finally, we conclude our work in Section 6.

2 Methods

2.1 Experimental setup

The sample preparation and experimental setup is mostly identical to the one used recently by Clavería et al.[36] In short, human red blood cells were obtained from healthy donors by needle-prick and used within three hours. After appropriate preparation,[36] they are suspended in a phosphate buffered saline (PBS) and bovine serum albumin solution which has a viscosity of approximately 1 mPa s. The viscosity ratio of the cells is therefore $\lambda \approx 5$.[27] This value corresponds to the typical physiological value of healthy red blood cells in blood plasma.[61] The RBCs are pumped at room temperature through

rectangular, PDMS-based channels by a high-precision pressure device (Elveflow OB 1, MK II) with pressure drops ranging from 20 to 1000 mbar. The channels have a cross-section width of $L_y = (11.9 \pm 0.3)$ µm and a height of $L_z = (9.7 \pm 0.3)$ µm without any applied pressure drop and are thus similar to the vessel diameters found in the microvascular system.[62,63] Their length is approximately $L_x = 40$ mm. We use rectangular rather than cylindrical channels since they are easier to manufacture, are therefore prevalent in lab-on-a-chip devices[63,64] and have the merit that cells are not rotated randomly around their axis due to the missing rotational symmetry. The latter property greatly simplifies the microscopic observation and analysis of the RBCs.

The hematocrit (volume percentage of RBCs) in the reservoir before the inlet is always $\lesssim 1.0\%$, i.e. very low. Nevertheless, we find cells flowing in clusters as well as single cells. For the present work we have analyzed only the latter. To this end, previous experimental and theoretical results showed that the hydrodynamic interaction in a linear channel decays exponentially, and becomes negligible if the inter-particle distance is more than twice the channel width.[54,65,66] Considering that our channel has the dimensions ≈ 12 µm $\times$ 10 µm, cells can be considered as being single for distances $\gtrsim 25$ µm. We only used cells that were at least 40 µm apart from other entities.

We perform measurements at two locations along the channel, namely at the entrance ($x = 0$ mm) and at $x = 10$ mm downstream. Clavería et al.[36] showed that only minor differences occur between measurements at $x = 2$ mm and $x = 10$ mm, i.e. the cells are well converged at the latter position. This position is also consistent with other references[18,22,26] and our simulations as explained in the ESI.† Vessel lengths in-between bifurcations in the microvascular system are less than 1 mm, i.e. much shorter.[67] Nevertheless, this is not necessarily true for in vitro experiments or lab-on-a-chip devices, and the long-time behavior also holds information about the general intrinsic properties. The flowing RBCs are recorded by an inverted bright-field microscope (Nikon TE 2000-S) with an oil-immersion objective (Nikon CFI Plan Fluor 60×, NA = 1.25) and a high-resolution camera (Fastec HiSpec 2G) at a frame rate of 400 frames per second. The camera is aligned along the z-direction so that the photographs show the cells in the x–y-plane (compare Fig. 2). Hence, determination of the z-position is not possible, but also not absolutely necessary as our simulations always show a z-position of nearly 0 (see Section 5). We analyze the recorded image sequence with a custom MATLAB script that detects each projected cell shape and the corresponding 2D center of mass position. It additionally tracks the cell position over the image sequence to obtain the individual cell velocity. Considering the optical setup, we assume an uncertainty in the position measurements of $\pm s_P$ with $s_P = 0.1$ µm. The cell shapes are classified by hand.

2.2 Simulation setup

The numerical simulations mimic our experimental setup as far as possible. Hence, we place a single red blood cell in a rectangular channel as shown in Fig. 2. The channel has a
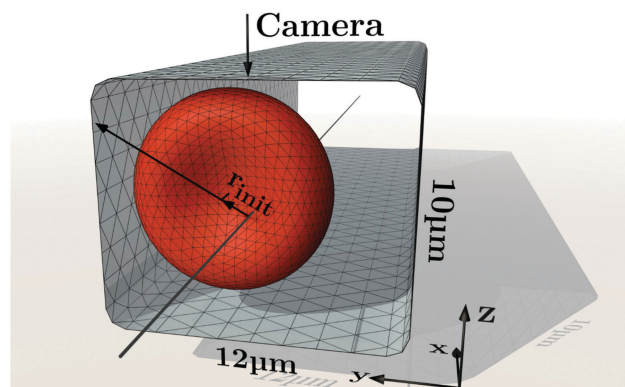

Fig. 2 Simulation setup: a single red blood cell is placed in a rectangular channel of width $L_y = 12$ µm and height $L_z = 10$ µm. Periodic boundary conditions are employed. Initially, the centroid of the cell is offset from the center axis along the left black arrow by a distance r_{init}. The depicted RBC illustrates the discocyte starting shape, although other shapes have been used, too, as explained in the main text and the ESI.† Furthermore, the black lines on the surfaces illustrate the employed meshes. The arrow at the top shows the view from the camera in the experiments (i.e. onto the x–y-plane) and the flow is in the positive x-direction.

cross-section of width $L_y = 12$ µm and height $L_z = 10$ µm. Periodic boundary conditions are assumed in the x-direction with a periodicity of $L_x = 42.7$ µm, in agreement with above estimates for the decay of hydrodynamic interactions.

We vary the initial y–z-position (relative to the channel center) of the RBC's centroid along the line $z_{init} = 5y_{init}/9$, which almost corresponds to the channel diagonal. The corresponding initial radial position is thus simply given by $r_{init} = \sqrt{y_{init}^2 + z_{init}^2}$. Apart from the initial position, we also vary the initial shape. The first employed shape is the typical discocyte equilibrium shape,[68,69] as depicted in Fig. 1(a), where the RBC axis is aligned with the channel axis (as shown in Fig. 2). The second and third starting shapes are a croissant and slipper, whose geometries are obtained from two simulations that start with a discocyte. They are further detailed in the ESI.†

Cell velocities are extracted by considering the difference of the centroids between successive time steps. During the simulation, we monitor several quantities such as the radial, y- and z-positions, the RBC asphericity and the cell velocity as well as the full 3D shape to determine when the steady state has been fully reached. The assumed shapes are classified manually by considering the 3D geometry and the graphs of the cell position, velocity and asphericity, similar to ref. 4. For example, slippers are off-centered and show periodic oscillations in the graphs, while croissants are centered and have a static shape (also compare the ESI†).

Regarding the actual modeling of the constituents, the RBC is filled with a Newtonian fluid with a dynamic viscosity μ_{RBC}, whereas the ambient flow is a Newtonian fluid with the dynamic viscosity $\mu = 1.2$ mPa s of blood plasma.[70–72] We set the viscosity ratio $\lambda = \mu_{RBC}/\mu$ to a value of 5 in all simulations. The surface area of the RBC is set to 140 µm² and the volume is set to 100 µm³ (see e.g. ref. 71 and 73), leading to a large radius of $R_{RBC} = 4$ µm when the cell is in the typical discocyte

equilibrium shape (Fig. 1(a)). The mechanics of the infinitely thin membrane are governed by Skalak's law[74,75] for the in-plane elasticity with a shear modulus of $\kappa_S = 5 \times 10^{-6}$ N m^{-1}[76,77] and an area dilatation modulus of $\kappa_A = 100\kappa_S$. This value for κ_A ensures that the area changes remain below 2% in all cases. We take the reference state for the Skalak model to be the typical discocyte shape.[68,69] The membrane is additionally endowed with some bending resistance which is modeled according to the Canham–Helfrich law,[78–80] where the bending modulus is fixed to $\kappa_B = 3 \times 10^{-19}$ N m.[77,81] The spontaneous curvature is set to zero.

We use 2048 flat triangles to discretize the RBC in our numerical implementation. The forces are computed as described by Guckenberger et al.,[82] with Method C therein being used for the bending contribution. An unavoidable artificial volume drift of the cell is countered by adjusting the velocity to obey the no-flux condition and by a subsequent rescaling of the object.[83,84] Moreover, the channel is represented by 2166 flat triangles. The corners are rounded to prevent numerical problems (compare Fig. 2). Rather than prescribing a zero velocity at the channel walls, we use a penalty method for efficiency reasons with a spring constant of $\kappa_W = 1.9 \times 10^7$ N m^{-3}.[6,84] Increasing the triangle counts and the box length L_x did not change the results significantly.

The Reynolds number in the considered system is defined as Re $= 2R_{RBC}u_{max}\rho/\mu$. For a velocity of $u_{max} \leq 10$ mm s^{-1} and the density $\rho \approx 10^3$ kg m^{-3} of the ambient and inner liquid we therefore have Re < 0.1. Hence, the flow can be appropriately described using the Stokes equation. This allows us to employ the boundary integral method (BIM)[85] for 3D periodic systems.[84,86] Note that this method requires to prescribe a certain average flow through the whole unit cell instead of a pressure drop within the channel. The latter is unfortunately not easily accessible. We therefore compare with experiments by means of cell velocities. Continuing, the integrals are computed by a standard Gaussian quadrature with 7 points per triangle in conjunction with linear interpolation of nodal quantities and appropriate singularity removal for the single- and double-layer potentials.[84] Furthermore, we use the smooth particle mesh Ewald (SPME) method[87] to accelerate the computation of the periodic Green's functions; cutoff errors are kept below 5×10^{-5}. The resulting linear system is solved via GMRES[88] up to a residuum of 10^{-5}, and the kinematic condition is integrated in time using the adaptive Bogacki–Shampine algorithm[89] with the absolute tolerance set to $10^{-5}R_{RBC}$. When the run-times are normalized to a two-socket system with 28 cores, each simulation took 1 to 29 days, with an average of around 5 days. The phase diagrams below are formed by 329 of such simulations in total. Further details on the numerical method as well as verifications of the implementation can be found in our previous publications.[27,82,84,90]

3 Experimental results

We classify cells in the experiments either as croissants, slippers or "other" not uniquely identifiable or completely different shapes. Typical slipper and croissant shapes are shown in the photographs (b and e) of Fig. 1. See the ESI† for a collection of all images.

To systematically investigate the occurrence of the different shapes, we vary the imposed pressure drops from 20 to 1000 mbar. The corresponding cell velocities range from 0.14 mm s^{-1} to 10.6 mm s^{-1}, covering the whole physiological range in microchannels.[62,91,92] We consider the cells 10 mm away from the channel entrance where most of the cells reached a steady state.[36] Fig. 3(a) depicts the fraction of observed shapes as a function of the measured cell velocities, constituting our central result from the experiments. This distribution was obtained by considering typically more than 100 cells per imposed pressure drop. The average velocities were computed by averaging over all cells at a certain pressure drop, with the horizontal error bars showing the corresponding standard deviations σ_u in cell velocity. Not all velocities are the same because croissants and slippers have different velocities at otherwise identical flow conditions,[27] and because of the natural variations of cell properties such as elasticity and size, as also noted by Tomaiuolo et al.[23] See the ESI† for more details. Considering Fig. 3(a), high velocities obviously favor slippers while croissants are the most prominent for medium velocities. A pronounced peak exists from around 1 to 2 mm s^{-1}. Very small velocities produce mostly shapes that fall outside our simple two-state classification.

Fig. 3(b) illustrates the corresponding estimated probability density function of the center of mass y-position of the cells at the various pressure drops. This estimate was obtained from the measured y-positions by using the kernel density estimator as implemented in MATLAB R2017a (ksdensity) with a support of $[-6,6]$ μm and otherwise default settings. Thus, croissants and "others" occurring at lower velocities are centered in the channel, while slippers occurring at high velocities show a pronounced off-centered position. The assumed shapes therefore imply a certain y-position within the channel with slippers being off-centered and croissants centered. This is confirmed when analyzing the offset distribution separately for each shape class as shown in the ESI.†

From Fig. 3(a) it is tempting to conclude that the flow velocity is the major parameter that determines the RBC shape, with low velocities favoring centered and high velocities favoring off-centered flow positions. However, looking at the cell positions near the channel entrance (Fig. 4) we find that already upon entering the channel RBCs are not homogeneously distributed. At low velocities we observe a clear bias towards a centered initial position, with the distribution becoming approximately homogeneous only at the highest measured velocities. These experimental observations allow two distinct parameters as the reason for the dominance of the slipper shapes at high velocities: either the higher flow velocity itself or the more off-centered entry into the channel. To disentangle these two possibilities we now present numerical simulations whose geometry directly corresponds to the experimental setup.
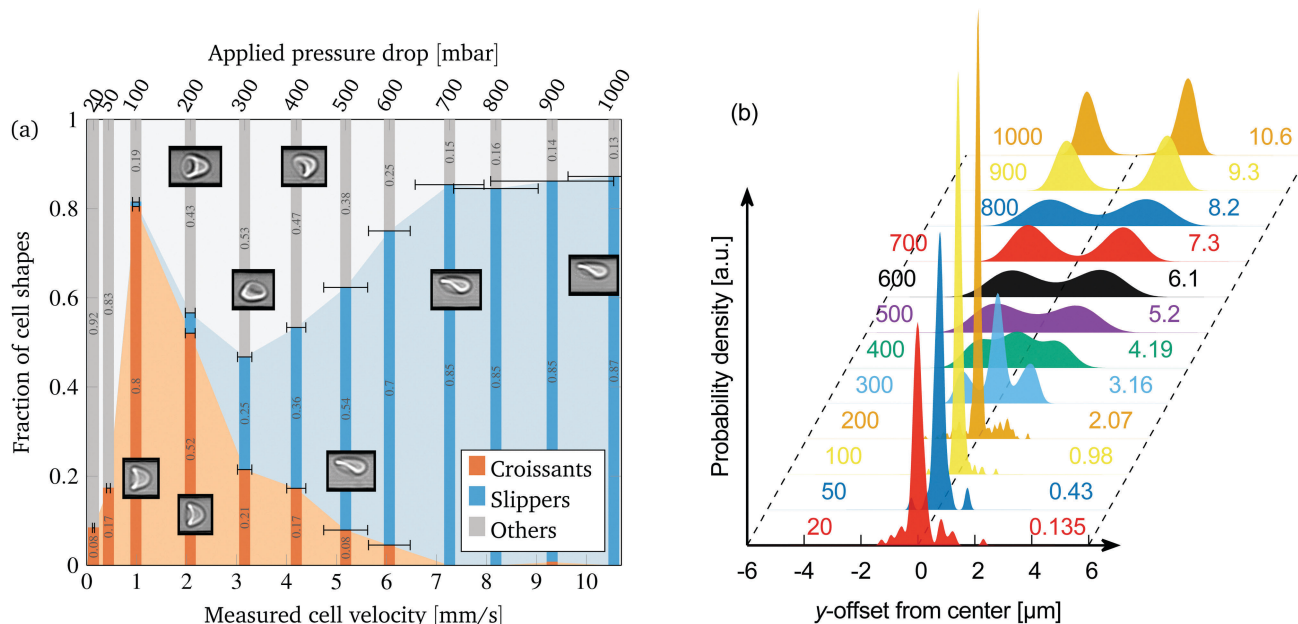
Fig. 3 Experimental results: (a) fraction of observed cell shapes as a function of the applied pressure drop (top axis) and mean cell velocity (bottom axis). The horizontal error bars depict the standard deviation of the measured cell velocities for each applied pressured drop. The shaded background is a guide to the eye. Furthermore, the insets show examples of experimental images (see the ESI† for a collection of all photographs). (b) Estimated probability density function of the RBCs' center-of-mass y-position within the channel for various pressure drops (indicated as numbers on the left in millibar) for all shapes combined. The corresponding measured mean cell velocities are depicted on the right in mm s^{-1}. We show the separated contributions of each shape to the distribution in the ESI.† The area under the curves is normalized to one. The dashed lines illustrate the wall positions. Both figures are for the position 10 mm downstream from the channel entrance.
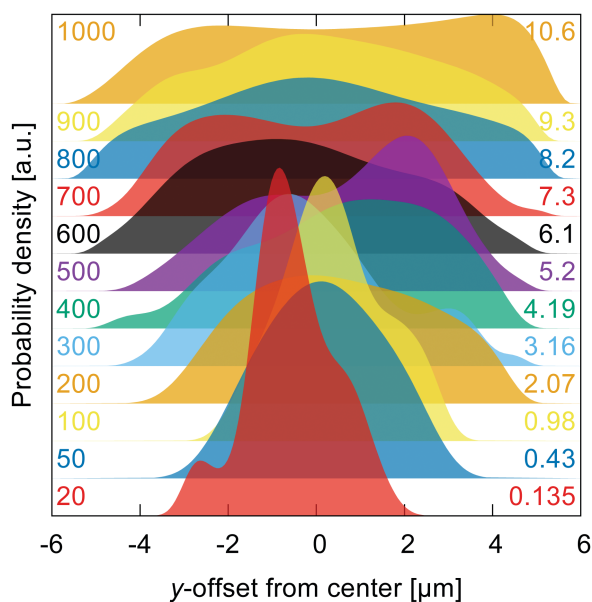

Fig. 4 Experimental results: estimated probability density function of the cells' center-of-mass y-position at the channel entrance (position $x = 0$ mm). The pressure drops increase from the bottom (20 mbar) to the top (1000 mbar) with the numbers on the left side indicating the corresponding value in millibar. We display the respective measured mean cell velocities in mm s^{-1} on the right side. The area under the curves is normalized to one. The curves are offset in the vertical direction for illustration purpose.

4 Numerical results

We numerically study the behavior of a single RBC in a rectangular microchannel by varying the imposed flow velocity, the initial shape and the initial offset r_{init} from the centerline of the tube (see Section 2.2). After starting the flow, we wait until the RBC reaches the steady state where the shape as well as the radial position does no longer change, or alternatively until periodic motion is observed.

In the majority of cases, we observe two different states: a croissant shape (which moves as a rigid body, Fig. 1(c)) and a slipper shape (Fig. 1(f)). The latter exhibits tank-treading (TT) and oscillatory contractions similar to the slippers seen by Fedosov et al.[4] (see the ESI† for a movie and the insets in Fig. 5). Tank-treading refers to the motion of the membrane around a (more or less) static shape. Note that perfectly axisymmetric parachutes are suppressed by the rectangular channel flow, contrary to the situation for cylindrical tubes[4] or unbounded Poiseuille flows.[17]

To start the systematic study, we take a red blood cell that is initially in the typical discocyte shape with its rotation axis aligned along the tube's axis (cf. Fig. 2). We then vary the radial offset r_{init} from the center line as described in Section 2.2 and record the final radial position as well as the shape. The mean of the radial position is extracted by a temporal average once the cell is in the steady state (see the ESI† for more details). Fig. 5 shows the result for a cell velocity of ≈ 6.5 mm s^{-1}. A single sharp transition
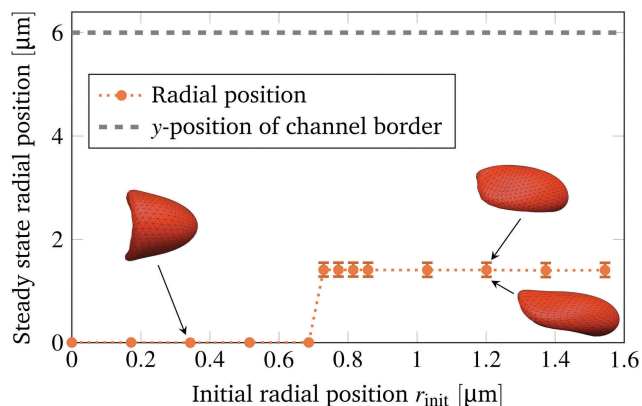
Fig. 5 Simulation results: averaged radial position in the steady state as a function of the initial radial offset for a cell velocity of ≈ 6.5 mm s^{-1}. The RBC starts in the typical discocyte shape with its rotation axis aligned with the tube's axis (Fig. 2). The dotted line is a guide to the eye. Half of the channel's extent along the y-direction (width) is shown as a dashed line at the top. The extent in the z-direction (height) is of less significance here since the steady states are always almost centered in the z-direction. Furthermore, the radial position for the converged slippers oscillates around a mean value and their shapes show periodic "contractions" as indicated by the vertical error bars and the right two insets, respectively.

at $r_{init} \approx 0.7$ μm from centered croissants to off-centered slippers is observed. The final position of the slippers is mostly offset only along the wider width of the channel (y-direction), but not along the smaller height (z-direction). Due to the transition we find pronounced bistability: the result is significantly determined by the initial condition and two different shapes (croissant and slipper) coexist. This is consistent with the 2D simulations by Secomb et al.[20] and Tahiri et al.[6] It also agrees qualitatively with observations by Farutin and Misbah for 3D simulations of vesicles in unbounded Poiseuille flow.[17]

To study the bistability in more detail, we vary the imposed flow velocity as well as the initial offset r_{init} and characterize the behavior in the steady state. This yields the shape phase diagram depicted in Fig. 6(a). The cell velocity is extracted in the steady state via a temporal average. For slippers the velocity varies periodically (similar to the radial position): the minimum and maximum in one period is indicated by the horizontal error bars. Overall, the mean cell velocity u ranges from 0.132 mm s^{-1} to 10.4 mm s^{-1}, matching with the experimentally covered range. The corresponding shear capillary number $Ca_S := \mu u / \kappa_S$ varies therefore in the interval $Ca_S \in [0.0317, 2.50]$, while the bending capillary number $Ca_B := \mu u R_{RBC}^2 / \kappa_B$ lies in the range $Ca_B \in [8.45, 666]$. The reddish area illustrates the approximated region where croissants exist. Furthermore, there is a maximal initial offset r_{init} above which overlapping with the vessel wall would occur.

The shape phase diagram in Fig. 6(a) (together with (b and c) explained below) constitutes our main result from the simulations. Starting near the channel center (in the reddish region) results in croissants, whereas higher initial offsets lead to slippers. The transition is found to be sharp, and depends significantly on the velocity. Croissants are the only stable steady state in a small region ranging from around 2 to 3 mm s^{-1}, independently of the initial radial position. Smaller and larger velocities tend to favor slippers. Stable croissants do not appear below 0.25 mm s^{-1}.

While the final shape is recognizable often early on, some small changes can still occur before the cell completely reaches the steady state. In the case of the slippers, the final perfectly periodic state is usually reached after roughly 2 s to 10 s. Relative to a typical flow timescale of $\tau := R_{RBC}/u$ (where u is the mean cell velocity), it is typically reached after 1τ to 500τ. In contrast, the final croissant state is in some cases achieved only after more than 30 s (i.e. $> 10^4 \tau$), possibly after an intermediate
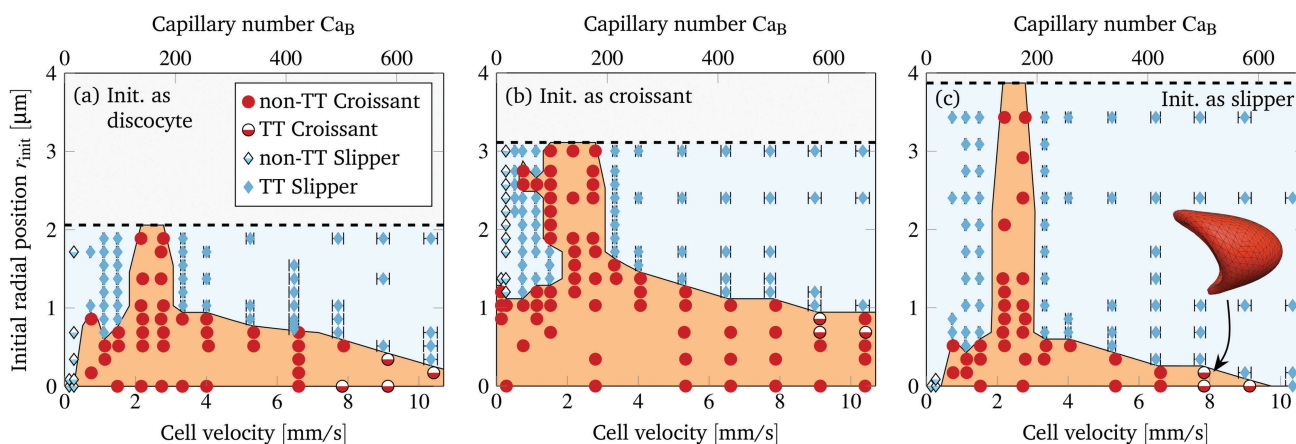

Fig. 6 Simulation results: shapes obtained when varying the initial offset r_{init} and the velocity. Each symbol corresponds to one simulation. The lower horizontal axis shows the average cell velocity in the steady state, while horizontal error bars depict the minimal and maximal velocities in one period (variations for croissants nearly zero and thus not visible). The upper dashed line represents the maximal initial offset: above this offset, the cell would overlap with the wall. The other lines and the colored areas are guides to the eye and illustrate the different regions in the phase diagram. Each figure corresponds to a different initial shape, namely (a) to the typical discocyte shape, (b) to a croissant and (c) to a slipper. These shapes are shown in Fig. 1(a) and in the ESI.† The inset in the last figure depicts an example of a tank-treading croissant. Fig. 5 corresponds to the vertical column at ≈ 6.5 mm s^{-1} in sub-figure (a).

slipper state that can last several seconds (see Fig. S7 and the movie in the ESI†). Hence, shapes observed in the simulations much earlier than one second can often turn out to be transient, contrary to the interpretation of Ye *et al.*[55] but in agreement with Prado *et al.*[25]

Considering our results in Fig. 6(a) in more detail, we find that two different types of croissants and slippers are possible. On the one hand, at very low velocities ($\lesssim 0.7$ mm s^{-1}) the slippers no longer exhibit tank-treading motion of the membrane and instead show tumbling behavior: the cell rotates around the z-axis while approximately preserving its shape (similar to a rigid-body, see the ESI† for a movie). The difference compared to the tumbling motion observed by Fedosov *et al.*[4] is that the cell still exhibits a clear slipper-like instead of a proper discocyte shape. Hence, we classify this mode still as slipper. On the other hand, at very high velocities ($\gtrsim 7$ mm s^{-1}) slightly asymmetric shapes strongly reminiscent of croissants with a distinct tank-treading motion can sometimes be observed (see the inset in Fig. 6(c) for an example). As the shape itself is very close to a croissant, we will nevertheless consider it to be a croissant below.

A natural question that occurs in light of the profound bistability is the influence of other initial shapes on the result. To this end, we consider a typical croissant as well as a typical slipper as the starting shape. Both were obtained from previous simulations that started with the discocyte form and are characterized in the ESI.† We once again construct the shape phase diagram as before and display the results in Fig. 6(b) and (c). Note that the different starting shapes admit a larger initial radial position r_{init} of the

centroid. In short, starting with a croissant favors croissants in the steady state (the reddish area is larger than in Fig. 6(a)). For slippers it is the other way around: starting with a slipper tends to produce more slippers (reddish area smaller than in Fig. 6(a)). Despite this, the croissant-only region from around 2 to 3 mm s^{-1} still exists unscathed. Overall, only two qualitative differences occur between the phase diagrams of different initial shapes, both at lower velocity when starting with the croissant shape (Fig. 6(b)): first, stable croissants emerge at very low velocities ($\lesssim 0.7$ mm s^{-1}) and second, the croissant-only peak exhibits a ''protrusion'' into the slipper space. This observation suggests that slippers and croissants can be stable below 2 mm s^{-1} for most r_{init} values. It is further confirmed by simulations that start with differently rotated discocytes in the ESI.†

Another interesting aspect concerns the radial positions of the centroids in the final steady states. The average values are obtained by computing the temporal average in the steady state first for each simulation, and then combining the results for identical shapes *via* a weighted arithmetic mean. We use the observation time in the steady state as the weight. This procedure leads to Fig. 7(a). Obviously, the final radial positions are independent of the initial starting shape, *i.e.* a particular steady state shape at a certain velocity is always located at the same position. Furthermore, non-tank-treading croissants are always almost centered, with only minor deviations away from zero. These slight deviations in the range from 2 to 4 mm s^{-1} are mainly due to some croissants exhibiting minuscule periodic shape deformations. Moreover, the centroids of tank-treading croissants occurring at velocities $\gtrsim 8$ mm s^{-1} are located near
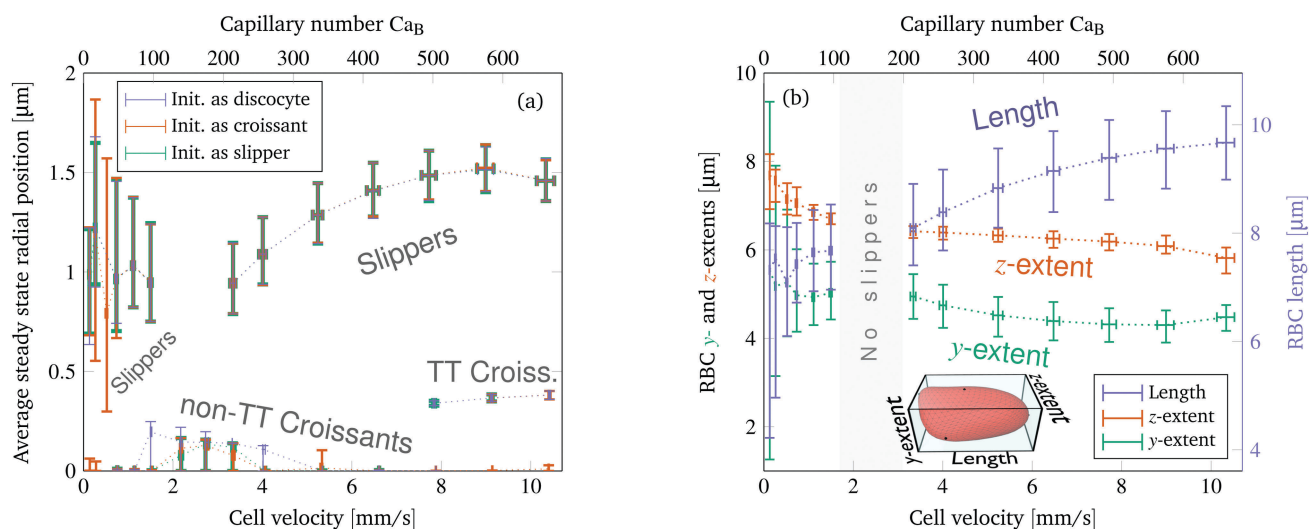

Fig. 7 Simulation results: (a) average radial positions of the steady states from Fig. 6 as a function of cell velocity for the three different starting shapes. The lower curves are for steady states forming non-TT croissants and TT croissants, the upper curves are for (TT and non-TT) slippers. Note that the data points coincide for different starting configurations, showing that the initial shape does not influence the final radial position. We show on the vertical axis the weighted temporal mean of the radial centroid position of RBCs that assume the same shapes. The vertical error bars depict the total minimal and maximal position, while the horizontal error bars show the total minimal and maximal cell velocities (in each period of the steady states, respectively). (b) Extents of the slipper shapes from figure (a) in the flow (x-)direction (length) and along the other two axes, as illustrated by the inset showing the channel-aligned bounding box around a slipper. The vertical error bars depict the minimum and maximum extents during the periodic contractions, while the horizontal error bars are the same as in (a).

but not directly in the center. Their slight off-centered position is a result of their asymmetry.

In contrast to croissants, slippers are located 0.8 to 1.5 μm away from the channel's axis. The minimum position is attained for velocities near the border of the croissant-only region in the phase diagram (at around 2 and 3 mm s^{-1}, compare Fig. 6). Above, the off-center position increases and seems to converge to a value of around 1.5 μm. The reason for this increase is that slippers become more elongated and thinner at higher velocities (up to a certain degree), as shown in Fig. 7(b) and also observed in previous experiments.[23] Thus, they effectively become thinner in the radial direction and their centroids can move closer to the wall. We note that the distance between the wall and the upper side of the slipper approximately remains the same for all velocities. This also hints at that the "optimal" off-center position for the slippers is more than 1.5 μm away from the center, and that this particular value is due to the smallness of the channel.

5 Comparison between experiments and simulations

5.1 Comparison of shapes

Considering Fig. 1, the croissants obtained from simulations and experiments look very similar, although the experimental shapes appear to be somewhat larger. The reason is diffraction: the "true" cell border lies in the bright and not within the dark rim. However, the slippers appear to look qualitatively different. This is due to the high magnification and numerical aperture of the objective which results in a small depth of field of around 1 μm. Cell borders above and below the middle plane are therefore blurred out and become invisible while the mid-plane cut becomes dominant. Thus, for comparison we should use the middle cross-section of the numerically obtained shapes. Here we find good agreement (compare Fig. 1(g) with Fig. 1(e)).

5.2 Comparison of the phase diagrams

A qualitative comparison between the phase diagrams of steady states from the experiments (Fig. 3(a)) and the simulations (Fig. 6) shows a striking resemblance: both exhibit a distinct peak in the number of croissants at lower velocities (1 to 3 mm s^{-1}) at the expense of the number of slippers. The latter dominate the picture at high velocities (>7 mm s^{-1}). At intermediate velocities both shapes coexist and can therefore be observed simultaneously in the measurements. Moreover, the simulations at very low velocities showed croissants only if the initial RBC was already prepared in that state, meaning that in the experiments this shape is highly unexpected. Indeed, we were not able to clearly classify most of the observed shapes in that regime as either croissants or slippers.

Obtaining a direct quantitative comparison requires a translation of the numerical threshold in Fig. 6 (which is in terms of the initial offset) into a prediction regarding the fraction of shapes, because the experimental diagram is in terms of the observed fraction of shapes. This is done by counting the fraction of croissants entering the channel with an offset below the numerical threshold. This fraction corresponds directly to the predicted fraction of croissant shapes. More precisely, we first define r_{trans} as the initial radial offset which separates croissants from slippers in the simulations by using the black line in Fig. 6. An exception is the small croissant-only region (i.e. the interval of the topmost horizontal line in Fig. 6) where we take $r_{trans} \to \infty$. This is consistent with our interpretation that only croissants exist in this particular interval. One r_{trans} is computed for each experimental cell velocity from Fig. 3(a). Second, each radial position r_{trans} is projected onto the y-axis to give y_{trans} (see Section 2.2) because only the y-offset is known from experiments. Third, from the experimental offset distribution at the channel entrance (Fig. 4) we can then estimate the fraction of cells ϕ that enter the channel with an offset below y_{trans}. Accordingly, the simulations predict a fraction ϕ of croissants in the steady state. The value of ϕ can thus be directly compared with the experimental phase diagram from Fig. 3(a). This is done once for every starting configuration employed in the simulations.

Fig. 8 shows this key result of our contribution, i.e. the predicted fraction of croissants ϕ as a function of the cell velocity for each starting shape. The vertical error bars depict the uncertainty in the prediction, whose computation is explained in the ESI.† They are comparably large in the croissant-only region because the experimental velocities lie very near its sharp boundary. The horizontal error bars illustrate the standard deviation σ_u of the experimentally measured cell velocities. Clearly, we find very good agreement between the prediction from the simulation and the experimental observation when considering the slipper starting shape (Fig. 8(c)). Starting with a discocyte or croissant leads to slightly more pronounced deviations (Fig. 8(a) and (b)), but still a satisfactory semi-quantitative agreement is maintained. This suggests the intuitive conclusion that the starting shapes in the experiment are closer to the rather asymmetric slippers than to the highly symmetric discocytes or croissants. Indeed, as explicitly shown in the ESI,† we only observe non-classifiable and rather asymmetric "other" shapes at the channel entrance.

As mentioned in the introduction, experimental investigations with more detailed shape studies are rather scarce. A comparison of the phase diagrams with the experimental literature is therefore limited to rough qualitative statements. Tomaiuolo et al.[23] found croissants and "others" for a cell velocity of 1.1 mm s^{-1} using $\lambda \approx 5$ in a cylindrical tube with diameter 10 μm. This is in agreement with our results. At 36 mm s^{-1}, slippers but also croissants have been observed. Since we cannot reach velocities that high, we can neither confirm nor refute the occurrence of the latter. Extrapolation of Fig. 8 is dangerous since the Reynolds number at 36 mm s^{-1} is around Re $\approx$ 0.24 and thus inertia effects might have noticeable contributions.[93,94] Continuing, Cluitmans et al.[26] found croissants and tumbling "others" at 1.1 mm s^{-1} and slippers at 13.6 mm s^{-1} in rectangular channels of 10 μm and 7 μm widths and a height of 10 μm, which is consistent with our results. The experimental phase diagram presented in ref. 22 and 21 also agrees with our results insofar that slippers occur at higher
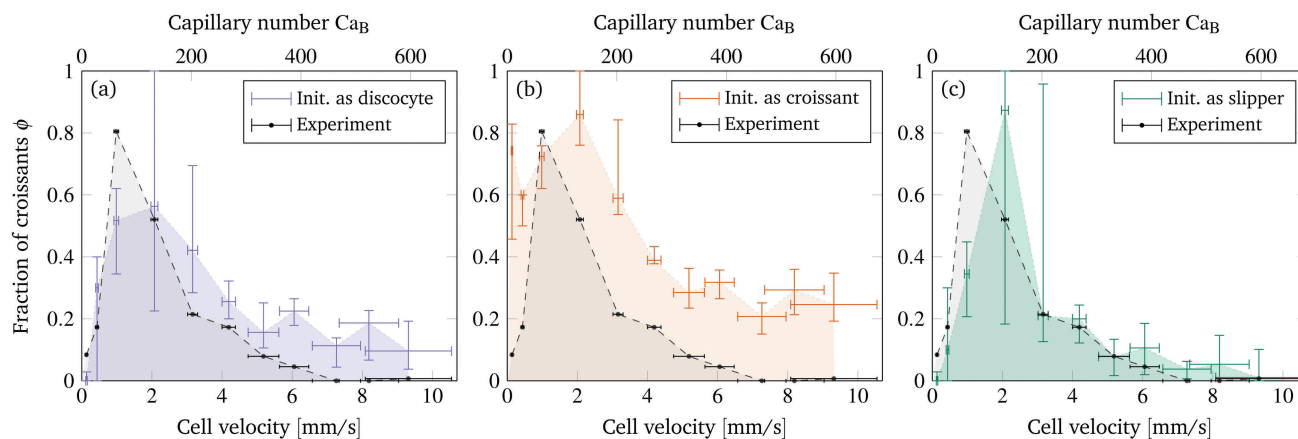
Fig. 8 Fraction of croissants ϕ predicted by the simulations, once for each starting configuration employed in the simulations: (a) simulations started with the typical discocyte, (b) with the croissant and (c) with the slipper shape. To allow for a direct comparison, we included the experimental results from Fig. 3(a) in each diagram (black dashed line). The horizontal error bars depict the standard deviation σ_u of the measured cell velocities (as in Fig. 3(a)), while the vertical error bars show the uncertainty in the prediction as explained in the ESI.† The lines and shaded areas serve as guides to the eye. See the main text for further details.

and croissants at lower velocities. Yet, the considered velocities were higher than 10 mm s^{-1} and the viscosity ratio was $\lambda \lesssim 0.27$, *i.e.* much lower. Furthermore, Fig. 3 in ref. 19 (*in vivo* experiments) also showed coexistence of croissants and slippers for velocities $\lesssim 1$ mm s^{-1} and only croissants in the range 1–2 mm s^{-1}, matching approximately with our results.

Regarding previous numerical studies, Fedosov *et al.*[4] performed detailed 3D numerical simulations in cylindrical channels for $\lambda = 1$. Taking a diameter of 10 μm (translating into a confinement value of $\chi = 0.65$ in their work), they varied the average velocity from around 0.05 mm s^{-1} to 0.7 mm s^{-1}. They observed a transition from snaking, to tumbling, to tank-treading slippers and finally to parachutes (which are very similar to croissants). In our simulations we found tumbling and tank-treading slippers at velocities of the order of 0.1 mm s^{-1}, and an increasing frequency of croissants above. This matches at least qualitatively with Fedosov *et al.*'s results. However, they did not vary the initial condition.

5.3 Comparison of cell positions

Next, we compare the preferred position of the cells in the steady state. The simulations predict a centered positioning of croissants (Fig. 7(a)), *i.e.* both the y- and the z-offsets are nearly zero. This matches with Fig. 3(b) where a very sharp peak at the channel center is found for the pressure drops within the croissant-peak region.

For slippers, the simulations showed an increase of the radial position of up to around 1.5 μm (Fig. 7(a)). Considering the y- and z-coordinates separately in Fig. 9, we see that $z \approx 0$ and the major offset happens in the y-direction. This is rather fortunate as the y-offset is also easily accessible in the experiments, contrary to the z-offset. As can be seen in the measured y-distribution (Fig. 3(b)), we have two off-centered peaks for slippers. Taking the distribution function for only the slippers, we extract the positions y_l and y_r of the two peaks. Exploiting the $\pm y$-symmetry of the channel, the off-centered position is
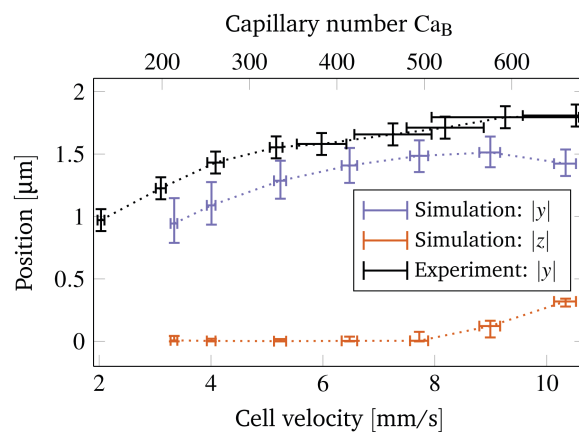

Fig. 9 Comparison between the centroid positions from the simulations (absolute values of the y- and z-coordinates) and experiments (absolute value of the y-coordinate) for cells that have a TT-slipper shape in the steady state. Error bars for the simulations as in Fig. 7(a). The horizontal error bars for the experimental data depict the standard deviation σ_u of the cell velocities, while the vertical error bars represent the estimated uncertainty in the position determination.

then computed as $(y_r - y_l)/2$, *i.e.* in essence as the average of the two peak distances to the central minimum. Fig. 9 compares these values with the numerical results: the behavior is the same (an increase with velocity) and the predicted values show only a small systematic deviation of around ≈ 0.3 μm, *i.e.* of less than 4% of the RBC diameter $2R_{RBC}$. A possible reason is that the optically recorded boundaries of the RBC and the channel walls are somewhat blurry (compare the experimental images in Fig. 1).

5.4 Implications of the comparison

There has been quite some debate in the literature if the croissant (or parachute) shapes observed *via* light microscopy are indeed what they appear to be. Gaehtgens *et al.*[18] (Fig. 4 therein), for example, solidified the flowing RBCs with

glutaraldehyde and found that the croissant-like shapes were actually slipper-like. Skalak and Branemark[38] pointed out that such shapes can also be "edge-on" discocytes with a flattened back. Ultimately, to uniquely identify the forms one needs some method to record the full 3D geometry of the flowing cells (*e.g.* as in ref. 16, 27, 33 and 95–99). This is unfortunately very hard to implement in the present experimental setup. However, this missing information is complemented here by the numerical simulations which are in good agreement with the experiments and thus our interpretation of the shapes as croissants should be correct.

The good agreement furthermore implies that our red blood cell model and simulation method is fully appropriate for describing the flow of RBCs in a straight microchannel. More sophisticated methods including *e.g.* thermal fluctuations or surface viscosity[4,25,53,54,100,101] are, at least for the present geometry, not required. For croissants this is intuitive since membrane movement such as tank-treading is absent, for the tank-treading slippers it is somewhat less obvious.

6 Summary & conclusion

To summarize, we have performed *in vitro* experiments and 3D simulations of healthy red blood cells flowing in a microchannel. The viscosity ratio was approximately 5 and the flow velocities ranged from around 0.1 mm s^{-1} to 10 mm s^{-1} in both methodologies, corresponding to the typical conditions prevailing in the microvascular system. We found that both the flow velocity as well as the initial starting configuration (shape and offset from channel center) have a major impact on the final steady state of the cells. Using three different starting shapes (discocyte, croissant and slipper), we constructed the corresponding phase diagrams *via* simulations. In most cases the cells assumed one out of two different forms: either a centered croissant or an off-centered slipper. Interestingly, for most velocities bistability, *i.e.* a dependence of the final shape on the initial condition, was observed. Only in a small range of velocities (at around ≈ 1 mm s^{-1}) was the final shape found to be always a croissant. The experimental diagram showed very good agreement with the numerical result, especially when considering the simulations that used the rather asymmetric slipper as starting shape.

We thus conclude that the employed numerical RBC model can sensibly describe the cell behavior in the presented setup. Moreover, since we used physiological viscosity ratios and flow velocities, we speculate that croissants and slippers can occur in the microvasculature at the same set of system parameters not just as transients but rather that both are states which are intrinsically assumed by the cells. Our results are important for applications where the cells should be in a specific state (*e.g.* in lab-on-a-chip devices) and allow for a comprehensive validation of numerical models.

Conflicts of interest

There are no conflicts to declare.

References

1 J. B. Freund, *Phys. Fluids*, 2013, **25**, 110807.
2 J. Picot, P. A. Ndour, S. D. Lefevre, W. El Nemer, H. Tawfik, J. Galimand, L. Da Costa, J.-A. Ribeil, M. de Montalembert, V. Brousse, B. Le Pioufle, P. Buffet, C. Le Van Kim and O. François, *Am. J. Hematol.*, 2015, **90**, 339–345.
3 S. Salehyar and Q. Zhu, *Soft Matter*, 2016, **12**, 3156–3164.
4 D. A. Fedosov, M. Peltomäki and G. Gompper, *Soft Matter*, 2014, **10**, 4258–4267.
5 O. Aouane, M. Thiébaud, A. Benyoussef, C. Wagner and C. Misbah, *Phys. Rev. E: Stat., Nonlinear, Soft Matter Phys.*, 2014, **90**, 033011.
6 N. Tahiri, T. Biben, H. Ez-Zahraouy, A. Benyoussef and C. Misbah, *Microvasc. Res.*, 2013, **85**, 40–45.
7 G. Danker and C. Misbah, *Phys. Rev. Lett.*, 2007, **98**, 088104.
8 V. Vitkova, M.-A. Mader, B. Polack, C. Misbah and T. Podgorski, *Biophys. J.*, 2008, **95**, L33–L35.
9 D. A. Fedosov, W. Pan, B. Caswell, G. Gompper and G. E. Karniadakis, *Proc. Natl. Acad. Sci. U. S. A.*, 2011, **108**, 11772–11777.
10 T. Krüger, M. Gross, D. Raabe and F. Varnik, *Soft Matter*, 2013, **9**, 9008–9015.
11 M. Thiébaud, Z. Shen, J. Harting and C. Misbah, *Phys. Rev. Lett.*, 2014, **112**, 238304.
12 D. Katanov, G. Gompper and D. A. Fedosov, *Microvasc. Res.*, 2015, **99**, 57–66.
13 L. Lanotte, J. Mauer, S. Mendez, D. A. Fedosov, J.-M. Fromental, V. Claveria, F. Nicoud, G. Gompper and M. Abkarian, *Proc. Natl. Acad. Sci. U. S. A.*, 2016, **113**, 13289–13294.
14 E. Henry, S. H. Holm, Z. Zhang, J. P. Beech, J. O. Tegenfeldt, D. A. Fedosov and G. Gompper, *Sci. Rep.*, 2016, **6**, 34375.
15 O. Otto, P. Rosendahl, A. Mietke, S. Golfier, C. Herold, D. Klaue, S. Girardo, S. Pagliara, A. Ekpenyong, A. Jacobi, M. Wobus, N. Töpfner, U. F. Keyser, J. Mansfeld, E. Fischer-Friedrich and J. Guck, *Nat. Methods*, 2015, **12**, 199–202.
16 F. Merola, P. Memmolo, L. Miccio, R. Savoia, M. Mugnano, A. Fontana, G. D'Ippolito, A. Sardo, A. Iolascon, A. Gambale and P. Ferraro, *Light: Sci. Appl.*, 2017, **6**, e16241.
17 A. Farutin and C. Misbah, *Phys. Rev. E: Stat., Nonlinear, Soft Matter Phys.*, 2014, **89**, 042709.
18 P. Gaehtgens, C. Dührssen and K. H. Albrecht, *Blood Cells*, 1980, **6**, 799–817.
19 Y. Suzuki, N. Tateishi, M. Soutani and N. Maeda, *Microcirculation*, 1996, **3**, 49–57.
20 T. W. Secomb, B. Styp-Rekowska and A. R. Pries, *Ann. Biomed. Eng.*, 2007, **35**, 755–765.

21 M. Faivre, PhD thesis, Université Joseph-Fourier – Grenoble I, Grenoble, 2006.

22 M. Abkarian, M. Faivre, R. Horton, K. Smistrup, C. A. Best-Popescu and H. A. Stone, *Biomed. Mater.*, 2008, **3**, 034011.

23 G. Tomaiuolo, M. Simeone, V. Martinelli, B. Rotoli and S. Guido, *Soft Matter*, 2009, **5**, 3736–3740.

24 G. Tomaiuolo and S. Guido, *Microvasc. Res.*, 2011, **82**, 35–41.

25 G. Prado, A. Farutin, C. Misbah and L. Bureau, *Biophys. J.*, 2015, **108**, 2126–2136.

26 J. C. A. Cluitmans, V. Chokkalingam, A. M. Janssen, R. Brock, W. T. S. Huck and G. J. C. G. M. Bosman, *BioMed Res. Int.*, 2014, e764268.

27 S. Quint, A. F. Christ, A. Guckenberger, S. Himbert, L. Kaestner, S. Gekle and C. Wagner, *Appl. Phys. Lett.*, 2017, **111**, 103701.

28 R. M. Hochmuth, R. N. Marple and S. P. Sutera, *Microvasc. Res.*, 1970, **2**, 409–419.

29 V. Seshadri, R. M. Hochmuth, P. A. Croce and S. P. Sutera, *Microvasc. Res.*, 1970, **2**, 434–442.

30 V. P. Zharov, E. I. Galanzha, Y. Menyaev and V. V. Tuchin, *J. Biomed. Opt.*, 2006, **11**, 054034.

31 G. Tomaiuolo, V. Preziosi, M. Simeone, S. Guido, R. Ciancia, V. Martinelli, C. Rinaldi and B. Rotoli, *Ann. Ist. Super. Sanita*, 2007, **43**, 186–192.

32 S. Guido and G. Tomaiuolo, *C. R. Phys.*, 2009, **10**, 751–763.

33 S. S. Gorthi and E. Schonbrun, *Opt. Lett.*, 2012, **37**, 707–709.

34 L. Lanotte, G. Tomaiuolo, C. Misbah, L. Bureau and S. Guido, *Biomicrofluidics*, 2014, **8**, 014104.

35 G. Tomaiuolo, L. Lanotte, R. D'Apolito, A. Cassinese and S. Guido, *Med. Eng. Phys.*, 2016, **38**, 11–16.

36 V. Clavera, O. Aouane, M. Thiébaud, M. Abkarian, G. Coupier, C. Misbah, T. John and C. Wagner, *Soft Matter*, 2016, **12**, 8235–8245.

37 M. M. Guest, T. P. Bond, R. G. Cooper and J. R. Derrick, *Science*, 1963, **142**, 1319–1321.

38 R. Skalak and P. I. Branemark, *Science*, 1969, **164**, 717–719.

39 K. Kubota, J. Tamura, T. Shirakura, M. K. Imura, K. Y. Amanaka, T. Isozaki and I. Nishio, *Br. J. Haematol.*, 1996, **94**, 266–272.

40 G. Tomaiuolo, L. Lanotte, G. Ghigliotti, C. Misbah and S. Guido, *Phys. Fluids*, 2012, **24**, 1–8.

41 C. Wagner, P. Steffen and S. Svetina, *C. R. Phys.*, 2013, **14**, 459–469.

42 M. Brust, O. Aouane, M. Thiébaud, D. Flormann, C. Verdier, L. Kaestner, M. W. Laschke, H. Selmi, A. Benyoussef, T. Podgorski, G. Coupier, C. Misbah and C. Wagner, *Sci. Rep.*, 2014, **4**, 4348.

43 H. L. Goldsmith and J. Marlow, *Proc. R. Soc. London, Ser. B*, 1972, **182**, 351–384.

44 T. W. Secomb, R. Skalak, N. Özkaya and J. F. Gross, *J. Fluid Mech.*, 1986, **163**, 405–423.

45 T. W. Secomb, *Microvasc. Res.*, 1987, **34**, 46–58.

46 T. W. Secomb, R. Hsu and A. R. Pries, *Am. J. Physiol.: Heart Circ. Physiol.*, 2001, **281**, H629–H636.

47 T. W. Secomb and R. Skalak, *Microvasc. Res.*, 1982, **24**, 194–203.

48 B. Kaoui, G. Biros and C. Misbah, *Phys. Rev. Lett.*, 2009, **103**, 188101.

49 B. Kaoui, N. Tahiri, T. Biben, H. Ez-Zahraouy, A. Benyoussef, G. Biros and C. Misbah, *Phys. Rev. E: Stat., Nonlinear, Soft Matter Phys.*, 2011, **84**, 041906.

50 B. Kaoui, T. Krüger and J. Harting, *Soft Matter*, 2012, **8**, 9246–9252.

51 L. Shi, T.-W. Pan and R. Glowinski, *Phys. Rev. E: Stat., Nonlinear, Soft Matter Phys.*, 2012, **85**, 016307.

52 G. R. Lázaro, A. Hernández-Machado and I. Pagonabarraga, *Soft Matter*, 2014, **10**, 7195–7206.

53 H. Noguchi and G. Gompper, *Proc. Natl. Acad. Sci. U. S. A.*, 2005, **102**, 14159–14164.

54 J. L. McWhirter, H. Noguchi and G. Gompper, *Soft Matter*, 2011, **7**, 10967–10977.

55 T. Ye, H. Shi, L. Peng and Y. Li, *J. Appl. Phys.*, 2017, **122**, 084701.

56 G. Danker, P. M. Vlahovska and C. Misbah, *Phys. Rev. Lett.*, 2009, **102**, 148102.

57 B. Kaoui, G. Coupier, C. Misbah and T. Podgorski, *Houille Blanche*, 2009, 112–119.

58 D. Cordasco, A. Yazdani and P. Bagchi, *Phys. Fluids*, 2014, **26**, 041902.

59 Z. Peng, A. Mashayekh and Q. Zhu, *J. Fluid Mech.*, 2014, **742**, 96–118.

60 K. Sinha and M. D. Graham, *Phys. Rev. E: Stat., Nonlinear, Soft Matter Phys.*, 2015, **92**, 042710.

61 G. R. Cokelet and H. J. Meiselman, *Science*, 1968, **162**, 275–277.

62 A. S. Popel and P. C. Johnson, *Annu. Rev. Fluid Mech.*, 2005, **37**, 43–69.

63 B. Sebastian and P. S. Dittrich, *Annu. Rev. Fluid Mech.*, 2018, **50**, 483–504.

64 M. Toner and D. Irimia, *Annu. Rev. Biomed. Eng.*, 2005, 7, 77–103.

65 B. Cui, H. Diamant and B. Lin, *Phys. Rev. Lett.*, 2002, **89**, 188302.

66 H. Diamant, *J. Phys. Soc. Jpn.*, 2009, **78**, 041002.

67 A. Koller, B. Dawant, A. Liu, A. S. Popel and P. C. Johnson, *Am. J. Physiol.: Heart Circ. Physiol.*, 1987, **253**, H154–H164.

68 E. Evans and Y.-C. Fung, *Microvasc. Res.*, 1972, **4**, 335–347.

69 D.-V. Le, *Comput. Methods Appl. Mech. Eng.*, 2010, **199**, 2622–2632.

70 S. Chien, S. Usami, H. M. Taylor, J. L. Lundberg and M. I. Gregersen, *J. Appl. Physiol.*, 1966, **21**, 81–87.

71 R. Skalak, N. Ozkaya and T. C. Skalak, *Annu. Rev. Fluid Mech.*, 1989, **21**, 167–200.

72 T. W. Secomb, *Annu. Rev. Fluid Mech.*, 2017, **49**, 443–461.

73 Y. Kim, H. Shim, K. Kim, H. Park, S. Jang and Y. Park, *Sci. Rep.*, 2014, **4**, 6659.

74 R. Skalak, A. Tozeren, R. P. Zarda and S. Chien, *Biophys. J.*, 1973, **13**, 245–264.

75 T. Krüger, F. Varnik and D. Raabe, *Comput. Math. Appl.*, 2011, **61**, 3485–3505.

76 Y.-Z. Yoon, J. Kotar, G. Yoon and P. Cicuta, *Phys. Biol.*, 2008, **5**, 036007.

77 J. B. Freund, *Annu. Rev. Fluid Mech.*, 2014, **46**, 67–95.

78 P. B. Canham, *J. Theor. Biol.*, 1970, **26**, 61–81.

79 W. Helfrich, *Z. Naturforsch., C: J. Biosci.*, 1973, **28**, 693–703.

80 A. Guckenberger and S. Gekle, *J. Phys.: Condens. Matter*, 2017, **29**, 203001.

81 Y. Park, C. A. Best, K. Badizadegan, R. R. Dasari, M. S. Feld, T. Kuriabova, M. L. Henle, A. J. Levine and G. Popescu, *Proc. Natl. Acad. Sci. U. S. A.*, 2010, **107**, 6731–6736.

82 A. Guckenberger, M. P. Schraml, P. G. Chen, M. Leonetti and S. Gekle, *Comput. Phys. Commun.*, 2016, **207**, 1–23.

83 A. Farutin, T. Biben and C. Misbah, *J. Comput. Phys.*, 2014, **275**, 539–568.

84 A. Guckenberger and S. Gekle, *J. Fluid Mech.*, 2018, **836**, 952–997.

85 C. Pozrikidis, *J. Comput. Phys.*, 2001, **169**, 250–301.

86 H. Zhao, A. H. Isfahani, L. N. Olson and J. B. Freund, *J. Comput. Phys.*, 2010, **229**, 3726–3744.

87 D. Saintillan, E. Darve and E. S. G. Shaqfeh, *Phys. Fluids*, 2005, **17**, 033301.

88 Y. Saad and M. Schultz, *SIAM J. Sci. Stat. Comput.*, 1986, **7**, 856–869.

89 P. Bogacki and L. F. Shampine, *Appl. Math. Lett.*, 1989, **2**, 321–325.

90 A. Daddi-Moussa-Ider, A. Guckenberger and S. Gekle, *Phys. Rev. E*, 2016, **93**, 012612.

91 A. R. Pries, T. W. Secomb and P. Gaehtgens, *Am. J. Physiol.: Heart Circ. Physiol.*, 1995, **269**, H1713–H1722.

92 O. Baskurt, B. Neu and H. Meiselman, *Red Blood Cell Aggregation*, CRC Press, 2011.

93 B. Kaoui and J. Harting, *Rheol. Acta*, 2016, **55**, 465–475.

94 C. Schaaf and H. Stark, *Soft Matter*, 2017, **13**, 3544–3555.

95 N. C. Pégard and J. W. Fleischer, *J. Biomed. Opt.*, 2013, **18**, 040503.

96 N. C. Pégard, M. L. Toth, M. Driscoll and J. W. Fleischer, *Lab Chip*, 2014, **14**, 4447–4450.

97 V. K. Jagannadh, M. D. Mackenzie, P. Pal, A. K. Kar and S. S. Gorthi, *Opt. Express*, 2016, **24**, 22144–22158.

98 K. Kim, K. Choe, I. Park, P. Kim and Y. Park, *Sci. Rep.*, 2016, **6**, 33084.

99 C. K. Rasmi, S. Padmanabhan, K. Shirlekar, K. Rajan, R. Manjithaya, V. Singh and P. P. Mondal, *Appl. Phys. Lett.*, 2017, **111**, 243702.

100 G. Tomaiuolo, M. Barra, V. Preziosi, A. Cassinese, B. Rotoli and S. Guido, *Lab Chip*, 2011, **11**, 449–454.

101 A. Yazdani and P. Bagchi, *J. Fluid Mech.*, 2013, **718**, 569–595.